In-plane rigid-body vibration mode characterization with a nanometer resolution by stroboscopic imaging of a microstructured pattern

Patrick Sandoz[1], Jean-Michel Friedt[2], Emile Carry[1]

[1] *Département d'Optique PM Duffieux, Institut FEMTO-ST, UMR CNRS 6174, Université de Franche-Comté, 25030 Besançon Cedex, France and*

[2] *Association Projet Aurore, Université de Franche-Comté, Maison de l'Étudiant, Avenue de l'Observatoire, 25030 Besançon Cedex, France**

Abstract

This article introduces an improved approach for the characterization of in-plane rigid-body vibration, based on digital processing of stroboscopic images of the moving part. The method involves a sample preparation step, in order to pattern a periodic microstructure on the vibrating device, for instance by focused ion beam milling. An image processing method has then been developed to perform the optimum reconstruction of this *a priori* known object feature. In-plane displacement and rotation are deduced simultaneously with a high resolution (10^{-2} pixel and 0.5×10^{-3} rad. respectively). The measurement principle combines phase measurements – that provide the high resolution – with correlation – that unwraps the phase with the proper phase constants. The vibration modes of a tuning fork are used for demonstrating the capabilities of the method. For applications allowing the sample preparation, the proposed methodology is more convenient than common interference methods or image processing techniques for the characterization of the vibration modes, even for amplitudes in the nanometer range.

I. INTRODUCTION

The measurement of static or dynamic in-plane displacements is of acute relevance, eg for the characterization of micro-devices (MEMS, MOEMS)[1,2], the control of local probes in near-field scanning microscopy[3,4] or the detection of living cell motions[5]. Most analytical techniques are based on optical methods and first results were obtained with holographic or speckle interference set-ups[6–8]. The continuous improvement of solid-state semi-conductor devices allowed improved performances and automation of these methods. Laser Doppler vibrometry (LDV)[9,10] and electronic speckle pattern interferometry (ESPI)[11,12] have become reference techniques for the measurement of in-plane displacements in both static or dynamic regimes and for one point or full field analyses.

As an alternative to the quite sophisticated optical methods, several research groups have attempted the measurement of in-plane displacements by direct object observation and digital image processing. In these cases, the useful image texture is formed either by the object structure itself[13–16], by laser speckle[17], or by an artificial pattern[18]. In order to reach subpixel or submicrometer resolutions, high signal to noise ratios are required and scientific grade cameras are often preferred.

The detection of in-plane rotation is usually derived from the observation of the local displacement direction at different points, for instance by using a scanning interferometric method[19]. A direct access to in-plane rotation angle with a high resolution and for vibrating objects is still lacking.

Our proposed innovation is to perform simultaneous measurements of in-plane rigid-body displacement and rotation with a high resolution and with a low cost standard vision system. The method is based on a combination of phase analysis of peculiar spatial frequencies – that correspond to a periodic pattern printed on the object surface – and usual image correlation. A stroboscopic illumination allows the full characterization of the vibration modes of the device under investigation. The method is based on the processing of a set of periodic shapes printed on the vibrating target and observed with a sufficient contrast with respect to the sample background. Because of this necessary sample preparation, the method can not be applied to any kind of vibrating elements. Cells and most biological material can not be addressed by the proposed method. However, for many man-made devices, the required preparation can be integrated in the fabrication process or realized afterwards with minimal

disturbance of the device behavior.

The use of periodical patterns has been reported for the high resolution measurement of both one-dimensional[20,21] and two-dimensional displacements[22–24]. In a work reported previously[24] we have suggested the use of a set of periodic points as reference target. In that approach, the high resolution is obtained through wavelet transforms and spatial phase analysis, while the removal of 2π phase ambiguities is based on the detection of the pattern borders. The latter requires an excellent image quality for avoiding errors of a multiple of the pattern period and is well suited mainly for applications in which the dot pattern can be observed by transmission. If the dot pattern has to be observed in reflection, the border detection was found to be very sensitive to image defects, leading to large errors in position reconstruction. These problems are solved as follows: the high resolution is still provided by spatial phase analysis while the coarse position that is required for phase ambiguity removal results from image correlation. The method can be applied successfully to poor quality images of the dot pattern. The requirements on the vibrating object surface quality are then released and the potential field of application is significantly widened. For instance, the vibration modes of a quartz tuning fork were fully characterized through accurate measurements of both displacement and rotation. Excellent results were obtained either with a dot pattern directly milled on the prong surface or etched on a thin glass plate stuck on the prong end.

II. POSITION AND ORIENTATION MEASUREMENT

The challenge of position detection by vision is well known and is represented in Fig.1. In our case, the mobile object is processed to produce a high contrast pattern of regularly distributed dots. The object position is thus referenced by the coordinate system (c, x, y) formed by the center and axis of the dot pattern. Then the reconstruction of the object position, orientation and displacement requires the accurate location of the target image coordinate system (c', x', y') within the image sensor pixel frame referenced by the coordinate system (O, u, v).

[FIG. 1 about here.]

The *a priori* knowledge of the object features is used, taking advantage of the periodicity of the dot pattern. The image processing is based on digital analysis of spatial frequencies of the dot pattern. In fact, only the first spectral components – i.e. the fundamental frequencies – are used in the processing. So let us define the modulation of the target visibility $T(x,y)$ in the object plane as:

$$T(x,y) = [1 + cos(\frac{2\pi x}{\Delta_x}) \cdot rect(\frac{x}{N_x\Delta_x})] \cdot [1 + cos(\frac{2\pi y}{\Delta_y}) \cdot rect(\frac{y}{N_y\Delta_y})] \quad (1)$$

where Δ_x, Δ_y, N_x and N_y are the periods of the dot pattern and the number of dots in the x and y directions respectively; $rect(x/X)$ stands for the usual rectangle distribution of width X. In the detection plane, the target image $T'(x',y')$ is given by:

$$T'(x',y') = [1 + cos(\frac{2\pi x'}{\gamma\Delta_x}) \cdot rect(\frac{x'}{\gamma N_x\Delta_x})] \cdot [1 + cos(\frac{2\pi y'}{\gamma\Delta_y}) \cdot rect(\frac{y'}{\gamma N_y\Delta_y})] \quad (2)$$

where γ is the imaging system magnification. The target image is detected by the image sensor referenced in the (O,u,v) coordinate system. With respect to the image sensor, the coordinate system (c',x',y') appears with a rotation angle α. Then the target image as available numerically can be expressed by:

$$\begin{aligned} T'(u,v) = \delta(u-u_c, v-v_c) * [1 + cos(\frac{2\pi\,(u\,cos\,\alpha + v\,sin\,\alpha)}{\gamma\Delta_x}) \cdot rect(\frac{u\,cos\,\alpha + v\,sin\,\alpha}{\gamma N_x\Delta_x})] \\ \cdot[1 + cos(\frac{2\pi\,(-u\,sin\,\alpha + v\,cos\,\alpha)}{\gamma\Delta_y}) \cdot rect(\frac{-u\,sin\,\alpha + v\,cos\,\alpha}{\gamma N_y\Delta_y})] \quad (3) \end{aligned}$$

where (u_c, v_c) are the image coordinates of the dot pattern center and $*$ stands for the convolution operation. Figure 2 presents a part of the dot pattern image as recorded experimentally (cf. section III). The accurate location of the dot pattern center involves independent processing of the two dot pattern directions, as allowed by spatial filtering in the Fourier domain.

[FIG. 2 about here.]

The Fourier spectrum of the dot pattern image can be expressed as:

$$\begin{aligned} \widetilde{T}(\xi,\eta) = \frac{e^{-j2\pi\xi u_c}.e^{-j2\pi\eta v_c}}{4}.\{2\delta(\xi,\eta) + [\delta(\xi-\xi_x, \eta-\eta_x) + \delta(\xi+\xi_x, \eta+\eta_x)] * A(\xi,\eta)\} \\ *\{2\delta(\xi,\eta) + [\delta(\xi-\xi_y, \eta-\eta_y) + \delta(\xi+\xi_y, \eta+\eta_y)] * B(\xi,\eta)\} \quad (4) \end{aligned}$$

where ξ, η are reciprocal variables of u and v; $\xi_x = cos\,\alpha/\gamma\Delta_x$; $\eta_x = sin\,\alpha/\gamma\Delta_x$; $\xi_y = -sin\,\alpha/\gamma\Delta_y$; $\eta_y = cos\,\alpha/\gamma\Delta_y$ and:

$$A(\xi,\eta) = \frac{sin\,\pi\,(\xi\,cos\,\alpha + \eta\,sin\,\alpha)\,\gamma\,N_x\,\Delta_x}{\pi\,(\xi\,cos\,\alpha + \eta\,sin\,\alpha)} \quad (5)$$

$$B(\xi,\eta) = \frac{sin\,\pi\,(-\xi\,sin\,\alpha + \eta\,cos\,\alpha)\,\gamma\,N_y\,\Delta_y}{\pi\,(-\xi\,sin\,\alpha + \eta\,cos\,\alpha)} \tag{6}$$

Figure 3 presents the modulus of the Fourier spectrum of the dot pattern of Fig.2. This Fourier spectrum is made of 9 clearly separated main lobes and expressed as:

$$\begin{aligned} \widetilde{T}(\xi,\eta) = \frac{e^{-j2\pi\xi u_c}.e^{-j2\pi\eta v_c}}{4}.\{4\delta(\xi,\eta) \\ +\underline{2\delta(\xi-\xi_x,\eta-\eta_x) * A(\xi,\eta)} + 2\delta(\xi+\xi_x,\eta+\eta_x) * A(\xi,\eta) \\ +\underline{2\delta(\xi-\xi_y,\eta-\eta_y) * B(\xi,\eta)} + 2\delta(\xi+\xi_y,\eta+\eta_y) * B(\xi,\eta) \\ +[\delta(\xi-\xi_x,\eta-\eta_x) * A(\xi,\eta)] * [\delta(\xi-\xi_y,\eta-\eta_y) * B(\xi,\eta)] \\ +[\delta(\xi+\xi_x,\eta+\eta_x) * A(\xi,\eta)] * [\delta(\xi-\xi_y,\eta-\eta_y) * B(\xi,\eta)] \\ +[\delta(\xi-\xi_x,\eta-\eta_x) * A(\xi,\eta)] * [\delta(\xi+\xi_y,\eta+\eta_y) * B(\xi,\eta)] \\ +\delta(\xi+\xi_x,\eta+\eta_x)] * A(\xi,\eta)] * [\delta(\xi+\xi_y,\eta+\eta_y) * B(\xi,\eta)]\} \end{aligned} \tag{7}$$

[FIG. 3 about here.]

In Eq.(7) the center coordinates appear only in the pure phase term: $e^{-j2\pi\xi u_c}.e^{-j2\pi\eta v_c}$ applied to the other terms that are independent of the center position. Therefore the retrieval of the center coordinates requires the correct identification of this phase term. This operation can be carried out by processing any component of the Fourier spectrum provided that the phase term can be identified. In our case we choose to work with the fundamental dot pattern frequencies (ξ_x,η_x) and (ξ_y,η_y), as indicated in Fig.3, corresponding to the terms underlined in Eq.(7). We apply successively two spectral filters with a narrow bandwidth in order to extract the lobes centered on (ξ_x,η_x) and (ξ_y,η_y) respectively. By inverse Fourier transform of the filtered spectra we generate numerically two digital images Im_x and Im_y expressed by:

$$\begin{aligned} Im_x(u,v) = FT^{-1}\{\frac{e^{-j2\pi\xi u_c}.e^{-j2\pi\eta v_c}}{2} \cdot \delta(\xi-\xi_x,\eta-\eta_x) * A(\xi,\eta)\} = \\ \frac{1}{2}exp\{j2\pi[\xi_x(u-u_c)+\eta_x(v-v_c)]\} \cdot rect(\frac{u\,cos\,\alpha + v\,sin\,\alpha}{\gamma N_x \Delta_x}) \end{aligned} \tag{8}$$

$$\begin{aligned} Im_y(u,v) = FT^{-1}\{\frac{e^{-j2\pi\xi u_c}.e^{-j2\pi\eta v_c}}{2} \cdot \delta(\xi-\xi_y,\eta-\eta_y) * B(\xi,\eta)\} = \\ \frac{1}{2}exp\{j2\pi[\xi_y(u-u_c)+\eta_y(v-v_c)]\} \cdot rect(\frac{-u\,sin\,\alpha + v\,cos\,\alpha}{\gamma N_y \Delta_y})] \end{aligned} \tag{9}$$

The images Im_x and Im_y correspond to two perpendicular sets of N_x and N_y straight lines respectively and centered on the center coordinates (u_c, v_c) – i.e. with the same phase than the original dot pattern. The phase is directly available in the interval $(-\pi, \pi]$ from the numerical data. Fig.4 (resp. Fig.5) represents the line set given by the real part of Im_x (resp. Im_y) and the wrapped phase given by the argument of Im_x (resp. Im_y). We can observe the regular phase distribution on the line array while some perturbations appear in the image borders.

[FIG. 4 about here.]

[FIG. 5 about here.]

[FIG. 6 about here.]

We know that N_x (resp. N_y) periods correspond to a linear phase excursion of $(-\pi N_x, \pi N_x]$ (resp. $(-\pi N_y, \pi N_y]$) and that the phase at the center position is equal to 0. Since the argument of images Im_x and Im_y is limited to a $(-\pi, \pi]$ interval, the solution is not unique at this stage. The information issued from the wrapped phase is affected by ambiguities of $2k\pi$ (i.e. k periods where k is an integer) and is not suitable for direct center position identification. This wrapped phase contains only a fine definition of the straight lines position and must be completed by a coarse position determination for removal of the entire period ambiguity. Then, for the identification of the dot pattern position, it is necessary to reconstruct two absolute phase maps of excursion equal to $(-\pi N_x, \pi N_x]$ (resp. $(-\pi N_y, \pi N_y]$) and free from period ambiguities – i.e. adjusted to the actual dot pattern outlines. This operation is performed by using the following procedure: in a first step the phase is unwrapped with an arbitrary phase constant in order to obtain a linear phase variation over a significant area. Fig.6 presents the continuous phase maps resulting from the argument unwrapping of the central part of Im_x and Im_y. If displacements are known to be limited to a few pixels, then the appropriate area for this phase unwrapping can be chosen *a priori* as in our case. If displacements can be large (tens of pixels), the area suitable for phase unwrapping is driven by the modulus of Im_x and Im_y that determines coarsely the dot pattern location. These phase maps are then fitted by a plane surface at the least square sense. We obtain two phase

plane equations:

$$\phi_x(u,v) = X_0 + X_1\,u + X_2\,v \tag{10}$$

$$\phi_y(u,v) = Y_0 + Y_1\,u + Y_2\,v \tag{11}$$

where $X_0, X_1, X_2, Y_0, Y_1, Y_2$ are the estimated coefficients. The $2k\pi$ ambiguity affects only the zero order coefficients X_0 and Y_0. The coefficients X_1, X_2, Y_1, Y_2 determine the phase plane orientation and are yet representative of the actual phase distribution. From Eq.(8) and (9), they can be identified to the estimated values of ξ_x, η_x, ξ_y, η_y respectively. Therefore we can deduce the dot pattern image orientation and periods to be:

$$\gamma\Delta_x = [X_1^2 + X_2^2]^{-1/2} \tag{12}$$

$$\gamma\Delta_y = [Y_1^2 + Y_2^2]^{-1/2} \tag{13}$$

$$\alpha = tg^{-1}(\frac{X_2}{X_1}) = tg^{-1}(\frac{-Y_1}{Y_2}) \tag{14}$$

The vision system magnification can also be obtained from Eq.(12) and (13) if the actual dot pattern periods Δ_x and Δ_y are known accurately.

The final position estimation requires the removal of the $2k\pi$ phase ambiguities. This is performed by image correlation. A pattern of N_x by N_y dots is generated numerically with the orientation and periods provided by Eq.(12) through (14). The resulting pattern is then a filtered copy of the recorded dot pattern image centered at a chosen position. The 2D correlation of this simulated feature with the actually recorded image presents a maximum peak, as can be seen in Fig.7.

[FIG. 7 about here.]

This peak provides an estimate of the dot pattern center (u_{cor}, v_{cor}) with a resolution of one pixel – i.e. better than the ambiguity range of $\pm$ half a period. Therefore, this image center estimate is used for the removal of phase ambiguities. The unwrapped phase maps of Fig.6 are then shifted with the necessary multiple of 2π in order to obtain an unwrapped phase in the interval $(-\pi, \pi]$ at pixel (u_{cor}, v_{cor}). We obtain the correct value of phase plane coefficients X_0 and Y_0. Finally the dot pattern center position (u_c, v_c) is solution of:

$$\phi_x(u_c, v_c) = 0 = X_0 + X_1\,u_c + X_2\,v_c \tag{15}$$

$$\phi_y(u_c, v_c) = 0 = Y_0 + Y_1\,u_c + Y_2\,v_c \tag{16}$$

Eq.(15) and (16) correspond to the median lines of patterns Im_x and Im_y. They are perpendicular and intersect at the center position. The center position resulting from such phase computations benefits from both spatial frequency filtering and data averaging over a significant image area. The subpixel capability of the developed phase approach has already been demonstrated[24]. Here, the removal of phase ambiguities by correlation was found to be much more robust than the outline detection used before[24]. For instance, no difficulty was induced by the noise level and illumination non-uniformity of Fig.2, whereas it was very problematic for the former outline detection.

The following additional remarks regarding the limitation and possible extension of the proposed methodology may be pointed out:

- The angle is retrieved here modulo $\pi/2$ because of the symmetry of the dot pattern. Unambiguous 360 degrees determination can be obtained by breaking the dot pattern symmetry; for instance by removing one dot in a corner and identifying the right quadrant by correlation.
- The position could not be retrieved by correlation without preliminary angle determination. Therefore phase computations are necessary and furthermore provide a better resolution than image correlation.
- This processing can be seen as a two-dimensional extension of the method proposed by Takeda for single line demodulation in profilometry by fringe projection[25].

III. APPLICATION TO IN-PLANE VIBRATION MODE CHARACTERIZATION

The developed method for position measurement by vision was applied to the characterization of in-plane rigid-body vibration. We worked on a 32768 Hz quartz tuning fork of the kind used for scanning probe microscopy with shear force control. In these applications a sharp tip is vibrating close to the inspected surface with an amplitude related to the tip-surface distance. The monitoring of the tip vibration amplitude, as seen through the current associated with the direct piezoelectric effect, allows the servo-control of the vertical tip position. The surface topography that is reconstructed results from the integration of the tip-surface interaction over the whole tip displacement. Therefore high lateral resolutions require short tip displacements[26]. Our final goal is the tip vibration amplitude measurement,

but we began this study by characterizing a tuning fork commonly used for tip vibration excitation[27]. To this end the tuning fork was prepared in two different ways. Firstly, a dot pattern was etched on a thin aluminium layer covering a microscope coverslip. Then the dot pattern area was sawed and stuck on the prong ends. Secondly, a tuning fork was polished and processed by focused ion beam (FIB) for the direct milling of the dot pattern on the prong end surface. Both methods led to excellent results in agreement with each other. The resonance frequencies changed significantly (30087 Hz with the stuck dot pattern vs 33720 Hz for the FIB specimen for the fundamental mode) but the vibration amplitude remained very close (difference less than 2%). Experiments reported here concerns the FIB specimen. In this case the dot pattern period is $3\mu m$, as was attested by scanning electron microscopy. Therefore it could be used as a reliable size reference. The prong section is $320 \times 590\,\mu m^2$ while its length is $6\,mm$. The experimental set-up used is presented in Fig.8.

[FIG. 8 about here.]

The tuning fork (Radiospares: 547-6985) end face is observed by means of a 20 time magnification objective and a standard CCD camera (Sony XC-ST50). The illumination is strobed by a light emitting diode (LED) (Luxeon star/C LXHL-MWEA) with a duty cycle of 8%, while a frequency synthesizer (Tektronix AFG320) delivers the necessary control signals. There are two possible solutions for the observation of the prong amplitude:

- The LED is strobed at the tuning fork frequency; so the prong is observed while it is exactly at the same position for every period. A phase delay between the tuning fork excitation and the LED illumination has then to be introduced step by step in order to explore the prong displacement over one period.

- A slight frequency shift is introduced between the LED illumination and the tuning fork excitation; so there is a slight displacement of the prong between consecutive light pulses. The prong is then observed at a position varying continuously at a frequency given by the frequency difference between LED illumination and tuning fork excitation. In this case, each image of the prong corresponds to an integration of its position over a fraction of the period. This introduces a slight smoothing of the measured displacement whose effect increases with the frequency difference.

In our case, the LED was excited with a frequency shift of 2 Hz with respect to the tuning fork excitation. Therefore the apparent prong frequency is also 2 Hz and is sampled at the

25 Hz video rate of the CCD camera. This trade-off was chosen because a sufficient sampling rate of 12.5 points per period is kept, and because a signal to noise enhancement by signal filtering in the frequency domain is allowed since the information of interest is shifted at 2 Hz. This is of prime interest in order to get rid of lower frequency drifts due to environmental disturbances. In these operating conditions, the resulting displacement smoothing due to the 8% duty cycle of illumination and to the 2 Hz frequency shift remains small and was ignored in the following. If necessary those effects can be evaluated analytically and taken into account in the results.

[FIG. 9 about here.]

The different vibration modes of the tuning fork were analyzed, but we report only on results obtained with higher order modes since they introduce smaller displacements. They are therefore of interest for scanning probe microscopy and they are more difficult to measure. Fig.9 presents the prong displacement as reconstructed for three different excitation voltages and for the overtone shear mode ($f = 195410\,Hz$). Only the displacement along the vertical direction of the CCD camera is shown since the prong displacement is almost parallel to this direction. Each plot corresponds to 400 positions arising from the *a posteriori* processing of a sequence of 400 recorded images. At 250 mV excitation, as expected we observe clearly the 2 Hz frequency of the apparent prong motion. This 2 Hz signal is distorted, especially by a slow drift of the mean position attributed to remaining mechanical instabilities. The noise level can be estimated from the third plot corresponding to a recording without tuning fork excitation. The RMS displacement was found to be 5.23×10^{-3} and 5.64×10^{-3} pixel in the X and Y directions respectively; corresponding to actual rms. displacements of 2.4 and 2.1 nm respectively. These results clearly demonstrate the nanometer scale capabilities of the method, while the mechanical disturbances remain probably the main noise source in this measurement.

[FIG. 10 about here.]

At 50 mV excitation, the prong displacement does not appear in the plotted results. However, since the prong is known to be observed with an apparent frequency of 2 Hz, its displacements can be searched in the frequency domain. Fig.10 presents the power spectrum of the measured displacements of Fig.9. A sharp peak appears at 250 mV excitation as expected from the displacement plot. At 50 mV excitation, this tuning fork vibration peak is

still present in the spectrum but with a reduced amplitude. As expected, this peak disappears in the third spectrum since the tuning fork is not excited. This figure demonstrates the interest of the chosen solution for a frequency separation of the low frequency noise, due to the set-up instabilities, from the actual prong displacement. By performing a suitable bandpass filtering in the frequency domain, the vibration amplitude can be extracted from the noise.

[FIG. 11 about here.]

We thus reconstructed the calibration curve of the prong displacements for the overtone mode as presented in Fig.11 for both directions. We observe a linear dependence of the vibration amplitude against the excitation voltage. In these experimental conditions, the displacement axis is tilted by 4.9 degrees with respect to the vertical camera axis. Deviations from a straight line can be observed in the figure, especially at 5 V excitation. This behavior is a measurement artefact due to the actual image recording rate. The nominal video rate is 25 frames per second, but it appears that one or more images are lacking because of over load of the computer central unit. These missing images introduce phase discontinuities in the 2 Hz variation of the measured displacements that affect the efficiency of the frequency domain bandpass signal extraction. These artefacts were clearly correlated with the time diagram of the recorded image sequences and could be avoided by synchronizing the vision system in order to ensure a continuous recording of the image sequence.

[FIG. 12 about here.]

The rigid-body rotation of the inspected specimen is also accessed by the developped method. This is demonstrated in Fig.12 which presents the evolution of the angle α for a sequence of 400 images. This measurement was performed at a frequency of 181552 Hz – i.e. for a vibration mode involving a significant torsion of the prongs and for a 4 V excitation. The measured mean angle corresponds to the orientation of the dot pattern with respect to the pixel frame, while the angle variation shows the actual torsion of the prong. Again the 2 Hz frequency carrier allows a signal extraction by bandpass filtering. We were able to reconstruct the calibration curve of the rotation angle amplitude against the excitation voltage for this vibration mode, as represented in Fig.13. Again we observe a linear dependence with a measurement threshold of about 0.002 degrees.

[FIG. 13 about here.]

For these rotation measurements, we obtain two estimates of the angle α as given by Eq.(14). In practice, the noise level was found to be dependent on the selected estmation data: a lower noise level is obtained when the angle is estimated by processing the image data along columns (line pattern almost horizontal as in Fig.4) rather than along lines (Fig.5). This phenomenon is already known and is due to the unperfect electronic triggering of the video line-start signal. Indeed, columns are free from such a phenomenon since the column signal corresponds to the actual pixel structure without electronic processing.

IV. CONCLUSION

This paper reports an improved methodology for position measurement by vision based on the image processing of a dot pattern attached onto the target of interest. The dot pattern periodic structure allows bandpass filtering in the Fourier domain as well as phase computations and least square fitting. These features provide a very high position resolution, ie better than 10^{-2} pixel with a standard CCD camera. The in-plane rotation is also measured with a high resolution. However the periodic structure implies 2π phase ambiguities. For the removal of the latter, a dot pattern with the correct in-plane orientation is generated numerically and correlated with the recorded pattern. Then the reconstructed phase maps are adjusted with the necessary 2π multiples and the unambiguous pattern center is determined. This approach was found to be very robust and applicable to dot pattern images in presence of noise and surface defects.

The method was applied to the characterization of in-plane vibration modes of a quartz tuning fork. We use a stroboscopic illumination with a frequency shift of 2 Hz with respect to the tuning fork excitation. Then the detected vibration is observed with an apparent frequency of 2 Hz that allows a signal to noise ratio (SNR) enhancement by bandpass filtering in the Fourier domain. Vibration amplitudes are measured with the present set-up down to 2 nm. The sensitivity can still be improved by recording longer sequences of consecutive images in order to enhance the digital definition of the signal bandwidth and therefore the SNR. High frame rate camera could also be chosen in order to shift the signal band towards higher frequencies for a better rejection of low frequency environment disturbances.

The demonstrated method requires a sample preparation in order to obtain the suitable

dot pattern on the observed plane. This is a limitation in the range of applications of the technique. However this preparation is compatible with many characterization needs, especially in the field of microtechnology. The use of FIB milling for dot pattern etching involves the removal of very low matter volumes and therefore very small drifts of vibration properties. Furthermore, depending on the specimen complexity, the dot pattern realization could be integrated in the fabrication process and directly made available for device characterization, for instance in M(O)EMS developments.

Acknowledgments

We acknowledge the help of MIMENTO technological platform staff and especially Roland Salut for FIB milling our specimens.

---

* Electronic address: patrick.sandoz@univ-fcomte.fr; Electronic address: jmfriedt@lpmo.edu; Electronic address: emile.carry@univ-fcomte.fr

[1] A. Bossebeouf, S. Petitgrand, J. Micromech. Microeng. **13**, S23-S33 (2003).

[2] L. Salbut, in Optical Inspection of Microsystems, (ed. by W. Jupner), 201-215, Taylor & Francis, ISBN. 0-8493-3682-1, London (2006).

[3] C.C. Wei, P.K. Wei, W. Fann, Appl. Phys. Lett. **67**, 3835-3837 (1995).

[4] Y.T. Yang, D. Heh, P.K. Wei, W.S. Fann, M.H. Gray, J.W.P.Hsu, J. Appl. Phys. **81**, 1623-1627 (1997).

[5] A. J. Aryanosi, D. M. Freeman, Biophysical Journal **87**, 3536-3546 (2004).

[6] H.J. Tiziani, Optica Acta **18**, 891-902 (1971).

[7] D. Joyeux, S. Lowenthal, Optics Comm. **4**, 108-112 (1971).

[8] S. Hueha, K. Shiota, T. Okada, J. Tsujiuchi, Optics Comm. **10**, 88-90 (1974).

[9] Y. Yeh, H.Z. Cummins, Appl. Phys. Lett. **4**, 176-178 (1964).

[10] C. Rembe, G. Siegmund, H. Steger, M. Wörtge, in Optical Inspection of Microsystems, (ed. by W. Jupner), 245-292, Taylor & Francis, ISBN. 0-8493-3682-1, London (2006).

[11] S. Nakadate, T. Yatagai, H. Saito, Appl. Opt. **19**, 1879-1883, (1980).

[12] A. Svanbro, Appl. Opt. **43**, 4172-4177, (2004).

[13] C.Q. Davis, D.M. Freeman, Appl. Opt. **37**, 1299-1304, (1998).

[14] L. Oriat, E. Lantz, Pattern Recognition, **31**, 761-771, (1998).

[15] S. Roux, F. Hild, Y. Berthaud, Appl. Opt. **41**, 108-115, (2002).

[16] B. Serio, J.J. Hunsinger, B. Cretin, Rev. of Scient. Instr. **75**, 3335-3341, (2004).

[17] M. Sjödahl, L.R. Benckert, Appl. Opt. **32**, 2778-2784, (1993).

[18] S.J. Timoner, D.M. Freeman, Appl. Opt. **40**, 2003-2016, (2001).

[19] O. Holmgren, K. Kokkonen, T. Mattila, V. Kaajakari, A. Oja, J. Kiihamäki, J.V. Knuuttila, M.M. Salomaa, Ultrasonics symposium **2**, 1359-1362, (2004).

[20] J.S. Sirkis, T.J. Lim, Experimental Mechanics **31**, 382-388, (1991).

[21] Y. Surrel, N. Fournier, in Optical Inspection and Micromeasurements, (Ed. by C. Gorecky), Proc. SPIE, **2782**, 233-242, (1996).

[22] P. Sandoz, J.C. Ravassard, S. Dembelé and A. Janex, IEEE Trans. Instrum. Meas. **49**, 867-873 (2000).

[23] P. Sandoz, P. Humbert, V. Bonnans and T. Gharbi, French Patent No. 02 02547, Feb. 22nd, 2002.

[24] P. Sandoz, V. Bonnans and T. Gharbi, App. Opt. **41**, 5503–5511 (2002).

[25] M. Takeda, K. Mutoh, App. Opt. **22**, 3977–3982 (1983).

[26] J.-M Friedt, E. Carry, Z. Sadani, B. Serio, M. Wilm, S. Ballandras, 19th EFTF conference, Besancon, France, (April $21^{st} - 24^{th}$ 2005), 615–620.

[27] K. Karraï, R.D. Grober, App. Phys. Lett. **66**, 1842-1844, (1995).

V. FIGURE CAPTIONS

1. Fig.1: Principle of position measurement by vision. The mobile target is represented by the dot pattern referenced by (c,x,y) in the object plane; (c',x',y'): image of (c,x,y); (O,u,v): image sensor reference coordinate system.

2. Fig.2: Dot pattern as recorded on an inspected target.

3. Fig.3: Modulus of the Fourier spectrum of the dot pattern image.

4. Fig.4: Up: set of continuous lines given by the real part of Im_x; down: angle of Im_x.

5. Fig.5: Up: set of continuous lines given by the real part of Im_y; down: angle of Im_y.

6. Fig.6: Unwrapped phase planes on the image center. Up: from Im_x; Bottom: from Im_y.

7. Fig.7: Up: Results of image correlation between the recorded dot pattern image and the simulated one. Down: correlation profile along line 66.

8. Fig.8: Experimental set-up used; Focus is made on the end side of the prong where the dot pattern is strobed by the light emitting diode.

9. Fig.9: Reconstructed displacement of the prong for different excitation voltages (from top to bottom: 250 mV, 50 mV, 0 mV).

10. Fig.10: Power spectrum of the displacement distribution as measured for different excitation voltages (from top to bottom: 250 mV, 50 mV, 0 mV).

11. Fig.11: Reconstructed calibration curve of the prong displacement versus excitation voltage for the overtone mode and for the two directions.

12. Fig.12: Reconstructed angle for the torsion mode at 4V excitation.

13. Fig.13: Reconstructed calibration curve of the prong rotation amplitude versus excitation voltage for the torsion mode. The insert illustrates the prong torsion in this mode.

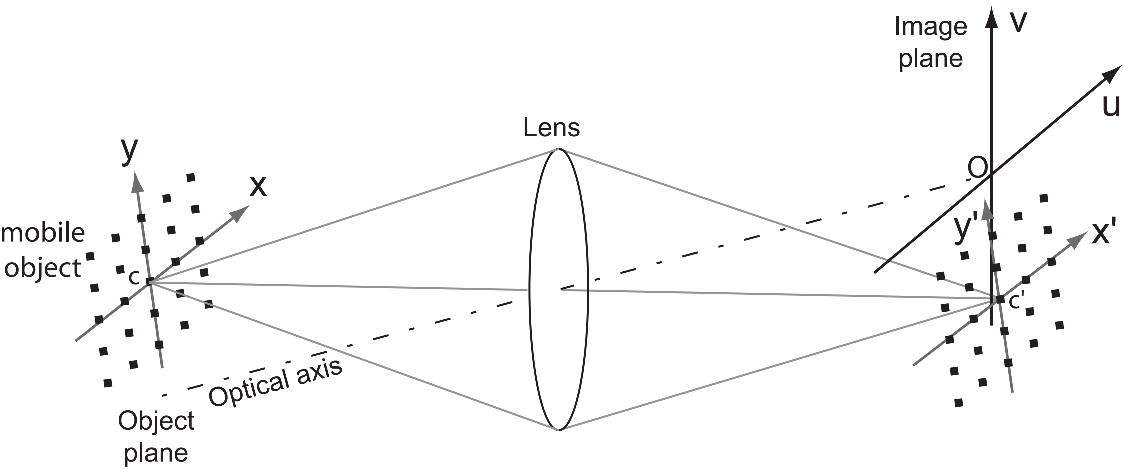
Image plane
v
u
O
Lens
y
x
mobile object
c
Optical axis
Object plane
y'
x'
c'

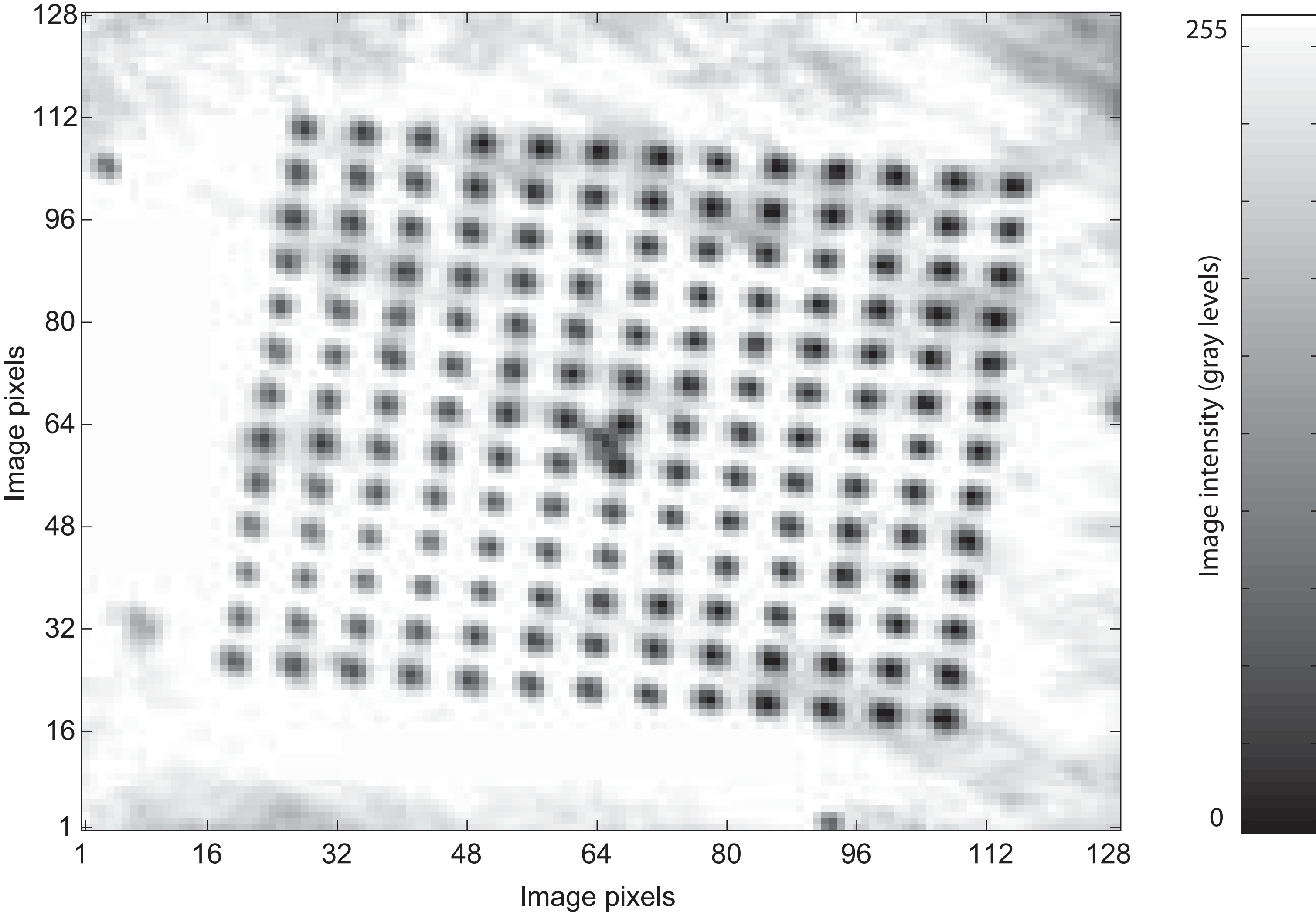

Image pixels
1
16
32
48
64
80
96
112
128
Image pixels
1
16
32
48
64
80
96
112
128
Image intensity (gray levels)
255
0

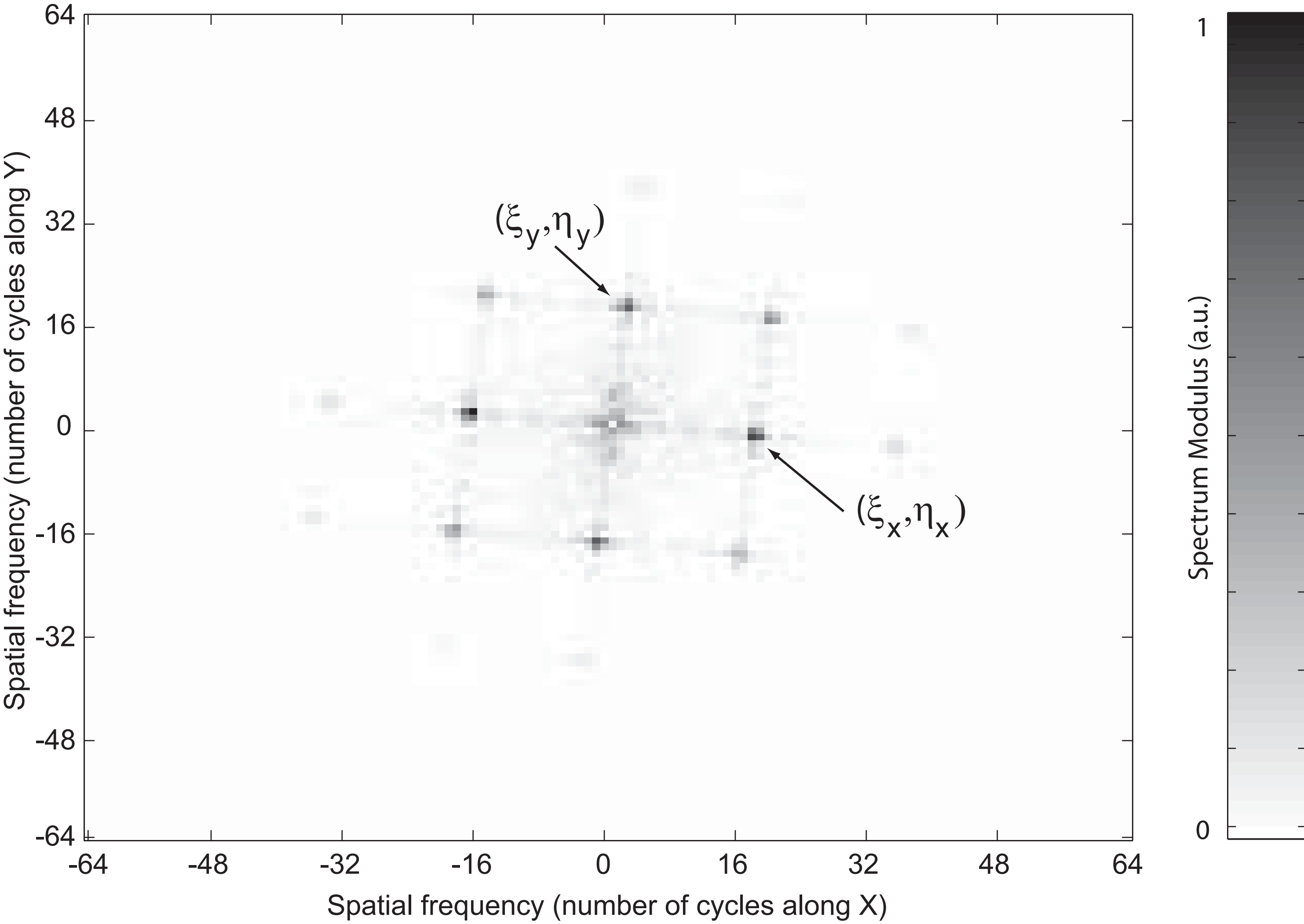

64
48
32
16
0
-16
-32
-48
-64
Spatial frequency (number of cycles along Y)
Spatial frequency (number of cycles along X)
(ξ_y,η_y)
(ξ_x,η_x)
1
0
Spectrum Modulus (a.u.)

Image intensity (gray levels)

128

0

Image pixels

1 16 32 48 64 80 96 112 128

Image pixels

1 16 32 48 64 80 96 112 128

Wrapped phase (rad.)

3.14

-3.14

Image pixels

1 16 32 48 64 80 96 112 128

Image pixels

1 16 32 48 64 80 96 112 128

128
112
96
80
64
48
32
16
1

Image pixels

1 16 32 48 64 80 96 112 128

Image pixels

128

Image intensity (gray levels)

0

128
112
96
80
64
48
32
16
1

Image pixels

1 16 32 48 64 80 96 112 128

Image pixels

3.14

Wrapped phase (rad.)

-3.14

Image pixels

Image pixels

(rad.)

Image pixels

Image pixels

(rad.)

(pixels)

(pixels)

Cross-correlation magnitude (a.u.)

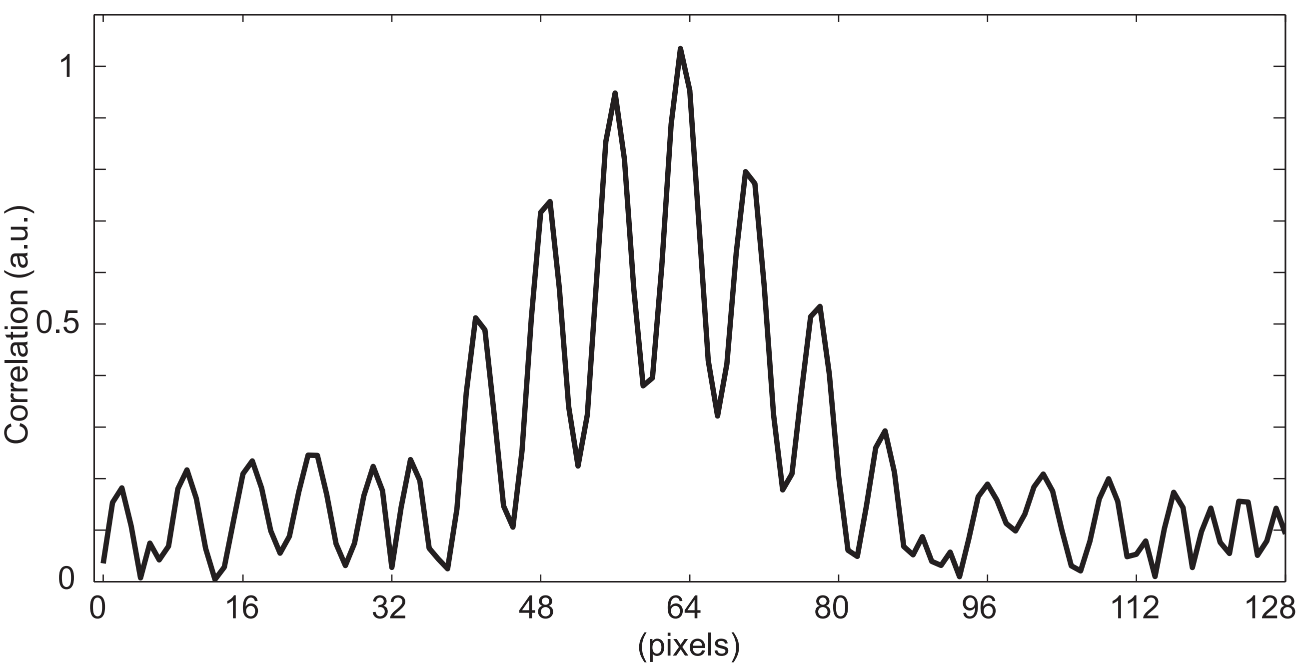

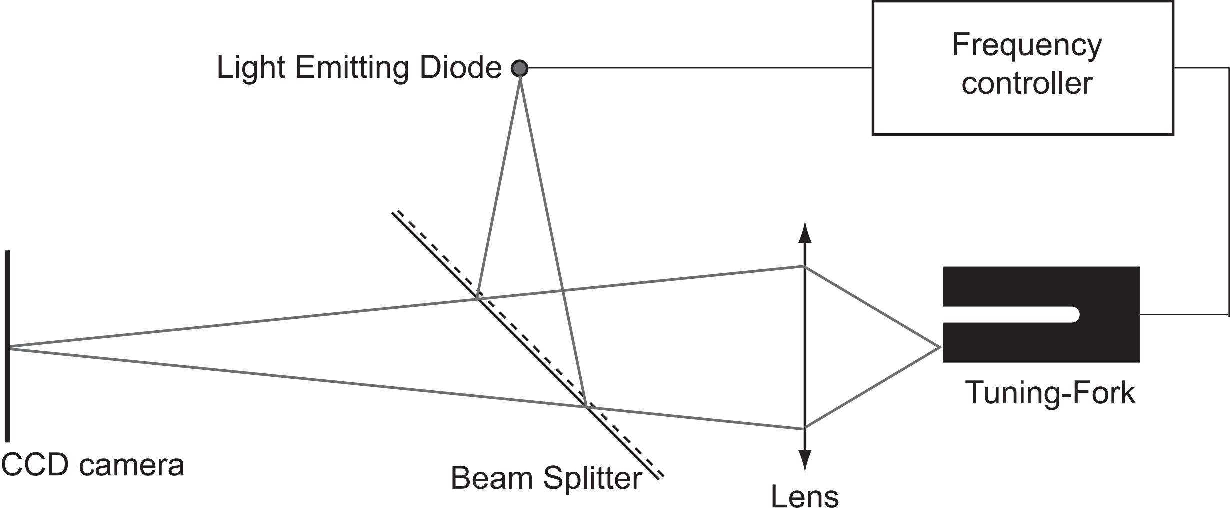
Light Emitting Diode
Frequency controller
Tuning-Fork
CCD camera
Beam Splitter
Lens

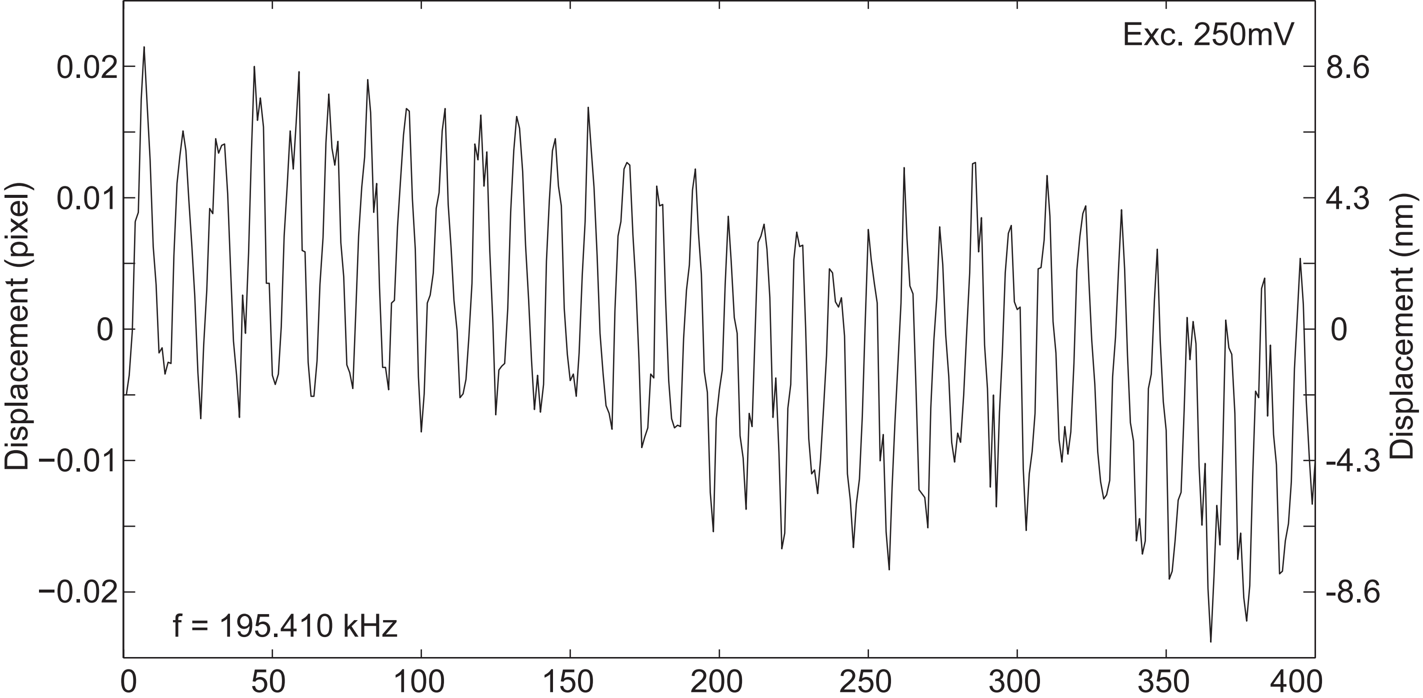

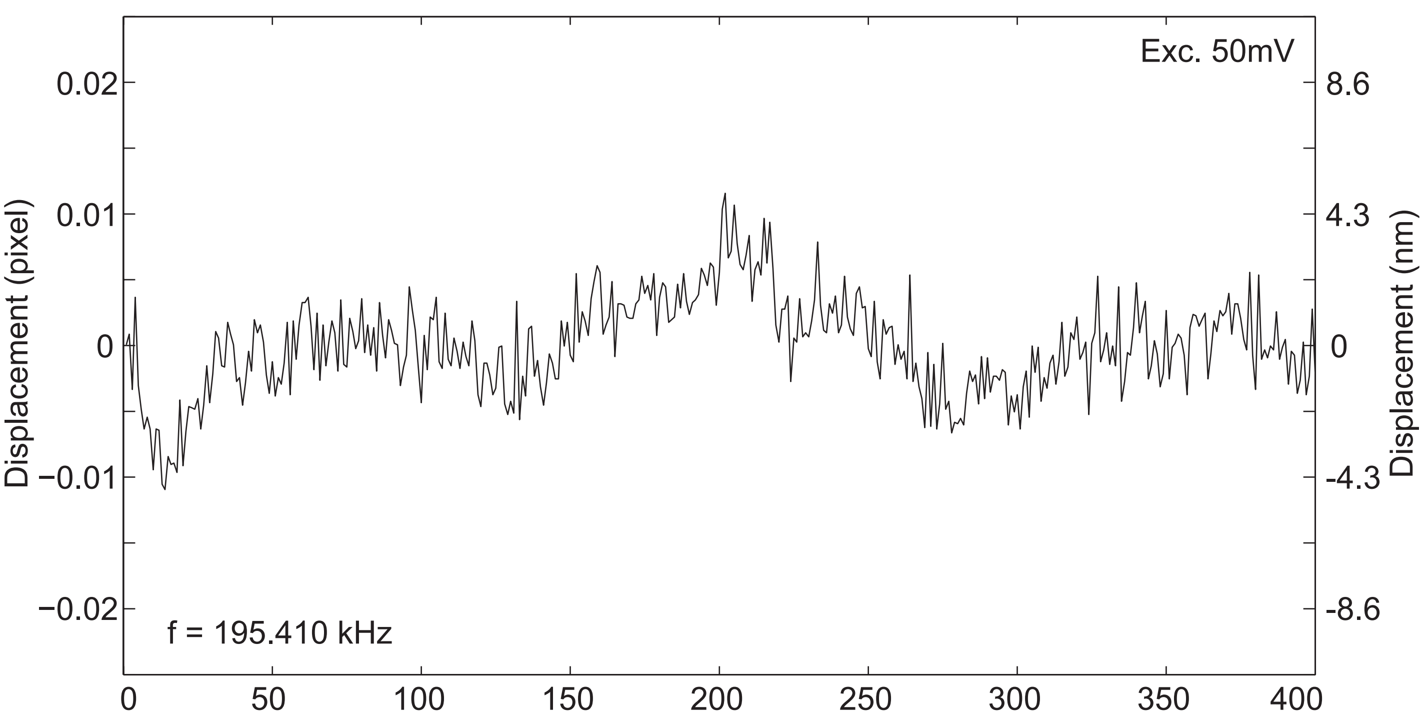

Exc. 0mV
Displacement (pixel)
Displacement (nm)
0.02
0.01
0
−0.01
−0.02
8.6
4.3
0
-4.3
-8.6
f = 195.410 kHz
0
50
100
150
200
250
300
350
400
Frame number (25 fr/s)

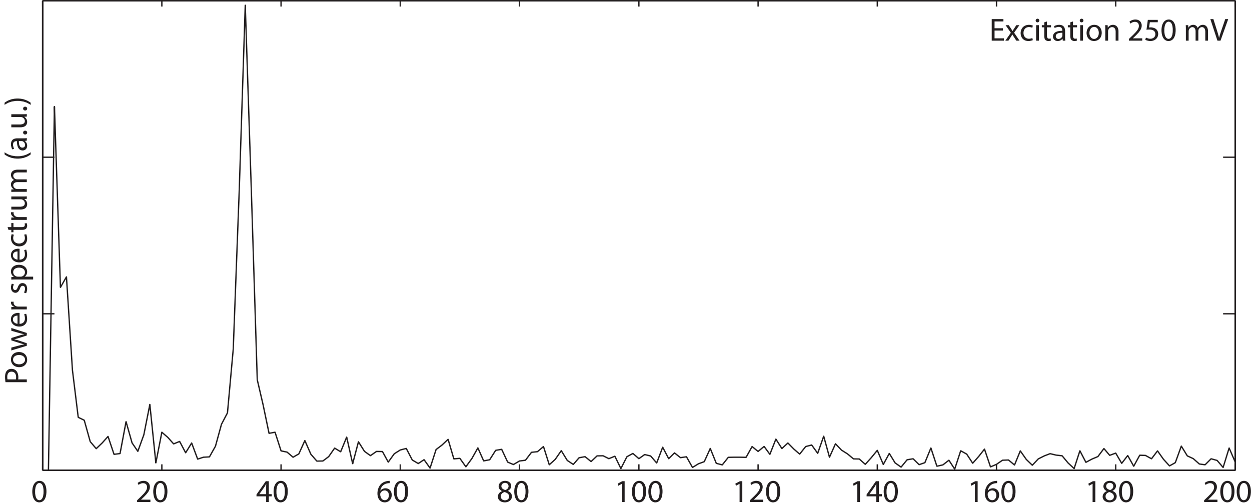

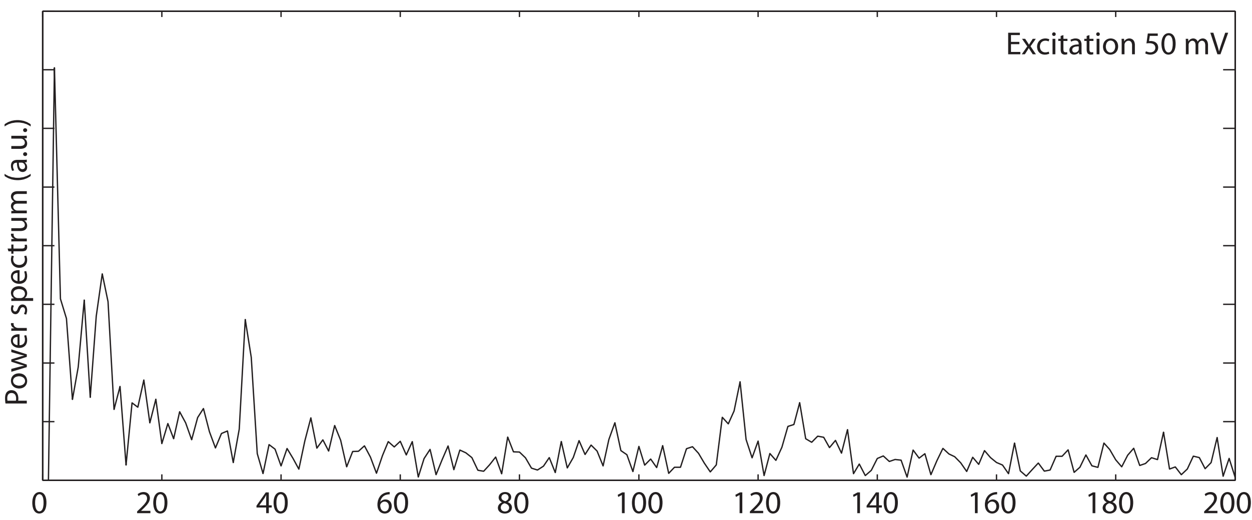

Excitation 0 mV

Power spectrum (a.u.)

0 20 40 60 80 100 120 140 160 180 200

Number of cycles in 400 frames

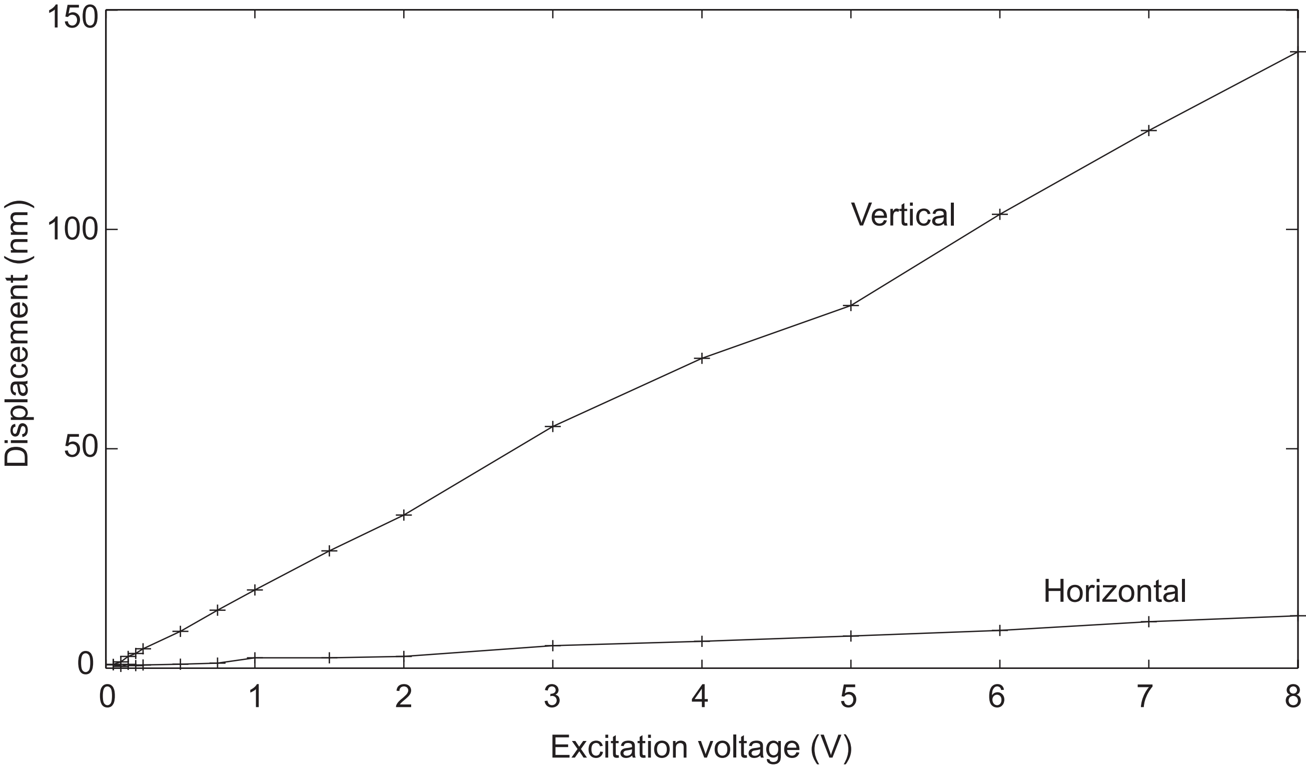
Displacement (nm)
150
100
50
0
Vertical
Horizontal
0
1
2
3
4
5
6
7
8
Excitation voltage (V)

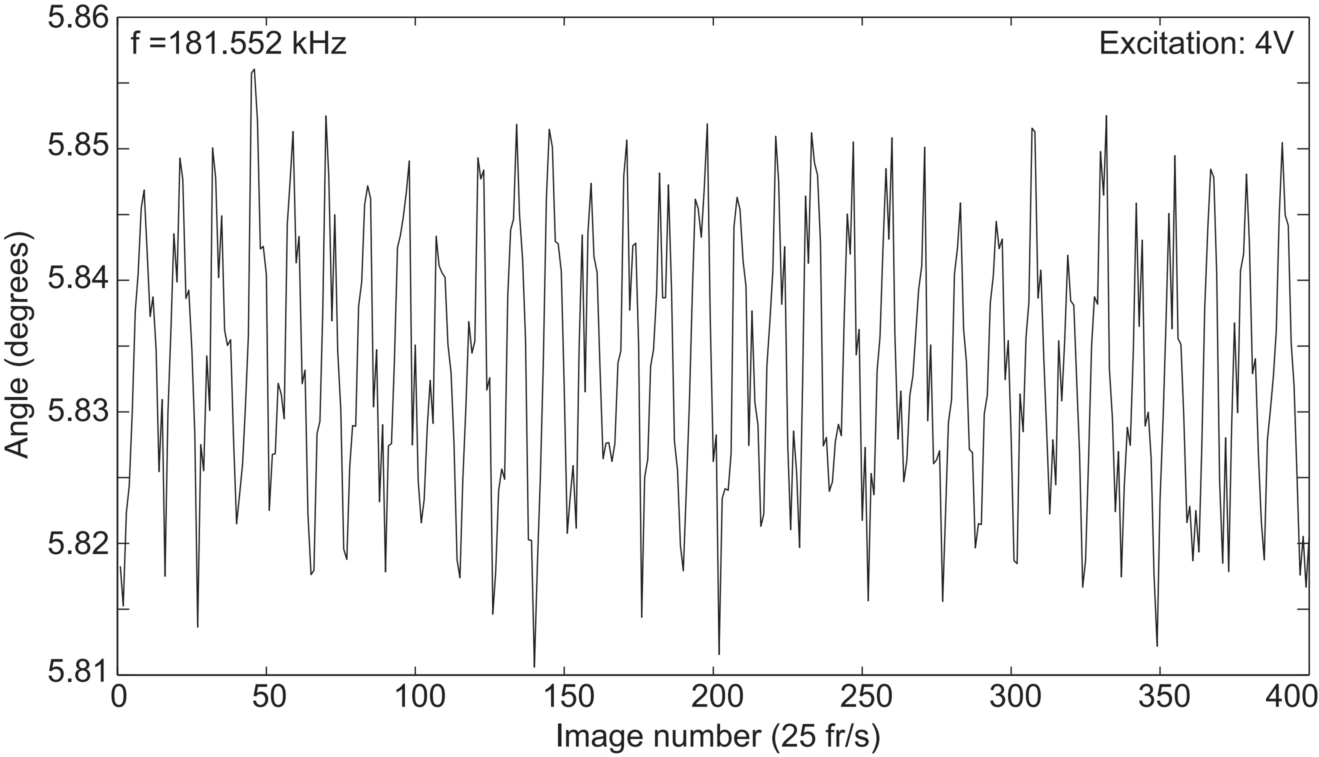

f =181.552 kHz
Excitation: 4V
Angle (degrees)
Image number (25 fr/s)
5.86
5.85
5.84
5.83
5.82
5.81
0
50
100
150
200
250
300
350
400

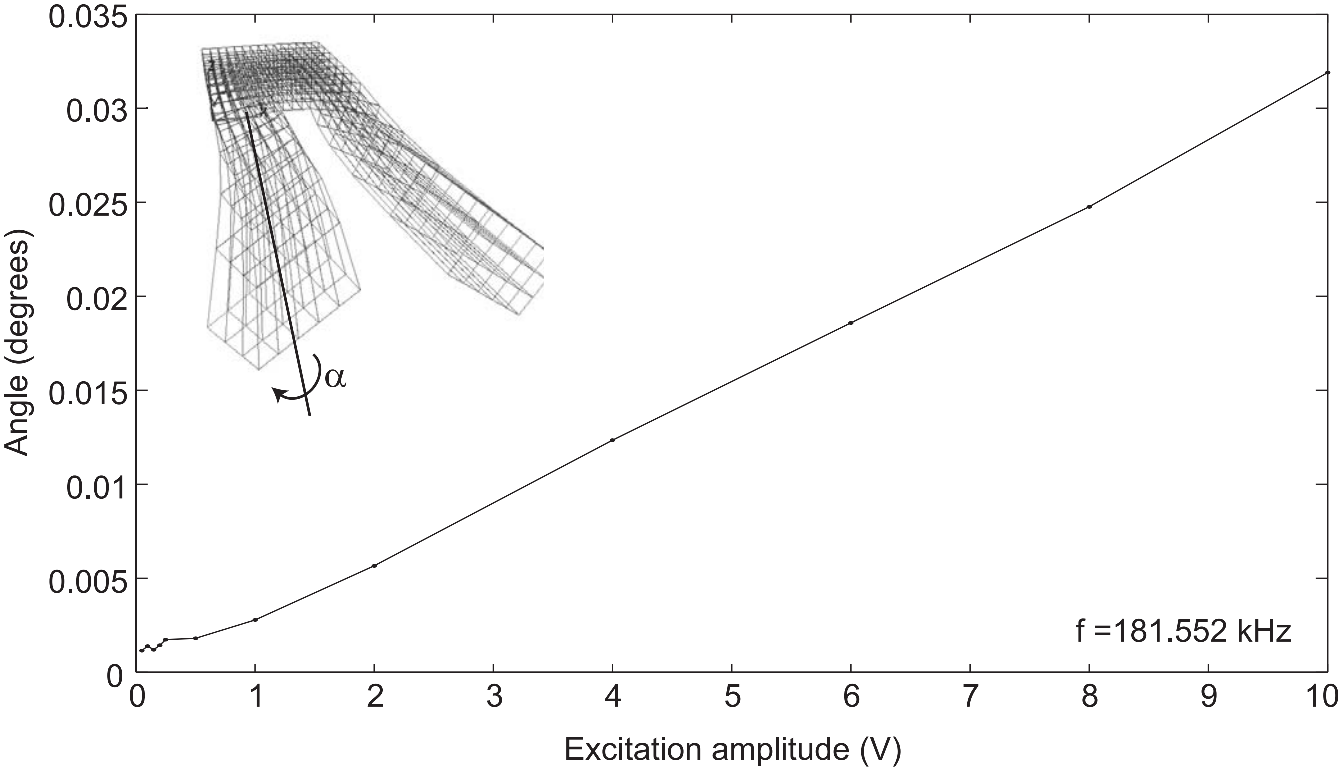

0.035
0.03
0.025
0.02
0.015
0.01
0.005
0
Angle (degrees)
0
1
2
3
4
5
6
7
8
9
10
Excitation amplitude (V)
f =181.552 kHz
α